Biomechanics and Modeling in Mechanobiology
https://doi.org/10.1007/s10237-020-01291-x

ORIGINAL PAPER

Computational modeling of the fluid flow in type B aortic dissection using a modified finite element embedded formulation

Rubén Zorrilla[1,2,3] · **Eduardo Soudah**[1,2] · **Riccardo Rossi**[1,2]

Received: 2 September 2019 / Accepted: 14 January 2020

Abstract
This work explores the use of an embedded computational fluid dynamics method to study the type B aortic dissection. The use of the proposed technique makes it possible to easily test different intimal flap configurations without any need of remeshing. To validate the presented methodology, we take as reference test case an in vitro experiment present in the literature. This experiment, which considers several intimal flap tear configurations (number, size and location), mimics the blood flow in a real type B aortic dissection. We prove the correctness and suitability of the presented approach by comparing the pressure values and waveform. The obtained results exhibit a remarkable similarity with the experimental reference data. Complementary, we present a feasible surgical application of the presented computer method. The aim is to help the clinicians in the decision making before the type B aortic dissection surgical fenestration. The capabilities of the proposed technique are exploited to efficiently create artificial reentry tear configurations. We highlight that only the radius and center of the reentry tear need to be specified by the clinicians, without any need to modify neither the model geometry nor the mesh. The obtained computational surgical fenestration results are in line with the medical observations in similar clinical studies.

Keywords Aortic dissection · Surgical fenestration · Phantom model · CFD · Embedded mesh methods · Level set methods · Bio-mechanics · Open source

1 Introduction

The aortic dissection (AD) is a cardiovascular disease that results from the tearing of the inner layer of the aortic wall. The blood flow emerging through the tear causes the dissection of the inner (intima) and middle (media) layers of the aorta. The AD is a very severe pathology which often becomes fatal when the blood-filled channel silently ruptures through the outer (adventitia) aortic wall. An early diagnosis and aortic wall resistance assessment are therefore required to prevent the AD to reach such catastrophic scenario.

ADs are classified according to the location of the dissection. Hence, those ADs located in either the ascending region of the aorta or the aortic arch are denoted as ascending ADs or type A ADs. On the contrary, those ADs located in the descending region of the aorta are denoted as descending ADs or type B ADs. Type A ADs typically require surgical interventions, while type B ADs commonly become in a chronic disease with a high long-term morbidity and mortality rates due to the recurrence, the progressive dilatation of lumen and the aortic rupture (Fattori et al. 2011). Type B ADs survival rate is around the 50–80% at 5 years and diminishes to the 30–60% at 10 years. This decrease in the survival expectation is associated with the progressive dilatation of the AD, which commonly has multiple causes. Some of these are the number, location and size of the intimal tears, the elasticity of the intimal flap (IF), the pressure difference between the true (TL) and false lumen (FL) or the high intraluminal pressure (Hartnell and Gates 2005) that may result in the rupture of the aortic tissue (Tolenaar et al. 2013).

Due to the severe, and possibly lethal, nature of the AD disease, it is crucial to quantify the pressure peaks, as well as to locate the points where the dissection tear jets impact. Unfortunately, it is very challenging to clinically measure

✉ Rubén Zorrilla
rzorrilla@cimne.upc.edu

[1] Centre Internacional de Mètodes Numèrics en Enginyeria, CIMNE, Barcelona, Spain

[2] Universitat Politècnica de Catalunya, UPC, Barcelona, Spain

[3] Present Address: CIMNE, C. Gran Capità s/n, Edifici B0, Campus Nord, UPC, 08034 Barcelona, Spain

Published online: 23 January 2020

these magnitudes as it requires the use of invasive techniques. In this context, numerical simulation and ex vivo experiments can play an important role in the study of the chronic AD evolution in order to prevent its possible lethal outcomes (Nauta et al. 2015). The hemodynamics of the AD disease have been extensively studied using either ex vivo models (Faure et al. 2014; Qing et al. 2012) or experimental phantoms (Tsai et al. 2008; Rudenick et al. 2013; Peelukhana et al. 2017; Marconi et al. 2017). However, numerical methods have been proved to be a valuable tool to assess the hemodynamics in AD phantom models (Soudah et al. 2015; Ben Ahmed et al. 2016) or to simulate real patient-specific AD scenarios (Wan AB Naim et al. 2014; Alimohammadi et al. 2015; Tse et al. 2011; Chen et al. 2016; Rudenick et al. 2010a; Ryzhakov et al. 2019). The majority of these works only consider the fluid dynamics problem, excluding the elastic effects in both the aortic walls and the IF (Soudah et al. 2015; Ben Ahmed et al. 2016; Tse et al. 2011).

A natural extension of these works is therefore to consider the IF as a flexible body, leading to the resolution of the AD as a coupled FSI problem. Despite the fact that this approach has been successfully applied in Alimohammadi et al. (2015), Chen et al. (2016) and Ryzhakov et al. (2019), its extension to real medical applications is limited as it is hardly possible to obtain, or even estimate, the mechanical properties of patient-specific IF tissues.

However, it is nowadays possible to efficiently provide a patient-specific aortic wall displacement field by using medical imaging techniques as the 2D and 4D-PC-MRI (Sherrah et al. 2017; Liu et al. 2018; Dillon-Murphy et al. 2016). This information can be used as input data to model the AD as a moving boundaries CFD problem. This means that the IF (and aortic wall) displacements are considered as boundary conditions (BCs) of the CFD problem, whose solution is thus influenced by the 'a priori' known boundary movement. The common approach to handle boundary movements is to use an arbitrary Lagrangian–Eulerian (ALE) framework (Hirt et al. 1974; Donea et al. 2004). Despite the ALE is possibly the most straightforward approach in these cases, it is known to suffer from large element distortion, or even inversion, when large boundary movements are involved (Bhardwaj and Mittal 2012).

It is also due consideration that the IF is an extremely thin wall with possibly space varying thickness. Hence, it makes sense to model the IF as a negligible thickness body. Unfortunately, dealing with such zero-thickness structures is particularly challenging from the preprocessing point of view as they require to duplicate their surface mesh in order to consider the 'positive' and 'negative' pressure sides. Moreover, the mesh generation in these cases is prone to fail as the polygonal representation of the surface mesh may intersect one of its duplicated counterpart due to the machine precision range operations.

Considering all the above-mentioned reasons, we decided to model the AD using an embedded mesh method, meaning that the negligible thickness IF is implicitly described by a level set function. This simplification implies that the entire AD volume of fluid is meshed disregarding the IF geometry, skipping thus all the previously mentioned preprocessing complexities (e.g., node and surface duplication) (Löhner et al. 2008). After the AD fluid volume has been meshed (background mesh), the IF geometry (skin) is superimposed to it to compute the level set function that implicitly represents it.

One of the main advantages of this technique is that there is no necessity to solve any mesh problem if the spatial configuration of the IF evolves in time. The unique requirement is thus to recompute the level set function according to the new IF configuration, which is assumed to be known from a position-time data set. This feature opens the possibility to easily model the flow of patient-specific AD scenarios with moving IF as it is nowadays straightforward to obtain the time evolution of the IF by using noninvasive medical imaging techniques such as the 4D-PC-MRI (François et al. 2013).

An extra motivation to use the presented embedded approach in the AD modeling scenario is the possibility to simplify the fluid flow assessment during the decision making before the fenestration surgical intervention. Aortic fenestration is a method to decrease high pressures in the hypertensive FL. This treatment is performed by creating an artificial tear in the IF with the objective of making possible the return flow from the FL to the TL. This change in the IF geometry reduces the FL intraluminal pressure, decreasing thus the dilatation risk of the FL. The use of the embedded approach offers the possibility of testing as many reentry tears as needed by only updating the level set function that describes it, requiring no modification nor remeshing in the background mesh. Thanks to this feature of the presented method, the new modified IF models can be straightforwardly set up.

This work is the first part of a new research line that aims to exploit embedded mesh methods for the more efficient assessment of the AD hemodynamics. One of the objectives of the present work is to prove that the AD CFD problem can be alternatively solved using embedded mesh methods, being their solution comparable to traditional body conforming (also known as body fitted) approaches in terms of accuracy and efficiency. To that purpose, we take as reference the work described in Rudenick et al. (2013) and Iwai et al. (1991), where several in vitro AD experiments are reproduced. It is due mentioning that there exists previous studies (Soudah et al. 2015; Ben Ahmed et al. 2016; Rudenick et al. 2010b) that also reproduced the in vitro experiments in Rudenick et al. (2013) which we take as reference. In all these publications the authors used an in-silico body

conforming CFD numerical approach. It is important to remark that in these in-silico experiments, the IF was considered to be a rigid body. This assumption explains the minor differences than can be appreciated when these results are compared with the experimental ones in Rudenick et al. (2013). The fact that the our reference works consider the IF as a rigid body as well as the absence of the IF displacement data in Rudenick et al. (2013) lead us to also take the rigid IF assumption.

Complementary, this work also aims to exploit the capability to easily generate different IF geometries to study surgical fenestration technique. Thus, we also present a handy method to artificially generate (and assess) the reentry tears by only setting the center and the radius of the new fenestration tears.

The paper is organized as follows. Section 2 describes the main concepts of the level set approach and presents the governing equations of the embedded CFD model used for the simulation of the AD. Next, in Sect. 3, geometry, fluid properties and boundary conditions corresponding to the considered AD cases are presented. In Sect. 4.1, the most significant results of the numerical simulations are summarized and compared with the reference data. In Sect. 4.2, we study the influence on the hemodynamics of a hypothetical AD surgical fenestration. Finally, Sect. 5 collects the main achievements and conclusions of the work and states the future work lines.

All the cases presented in this work are solved using Kratos Multiphysics, an Open Source C++ object oriented finite element framework for the resolution of multiphysics problems (Dadvand et al. 2010, 2013).

2 Formulation

2.1 Level set-based embedded approach

The most distinguishable feature of any embedded (or immersed) approach is the capability to decouple the geometry of the analyzed objects from the problem domain mesh. As opposite to the traditional body conforming (also known as body-fitted) approaches, these kind of formulations do not solve the problem using a discrete representation of the analyzed bodies but using a mathematical representation of them, which is typically achieved by using a level set technique.

The level set method, which was firstly proposed by Osher and Fedkiew in Osher and Fedkiw (2003), makes it possible to implicitly describe physical discontinuities occurring in a background mesh. This method has been successfully applied in a vast amount of engineering problems, ranging from the representation of the fluid interface in two-fluid (Sussman et al. 1994; Codina and Soto 2002) and free-surface (Rossi et al. 2013) problems to the tracking of crack paths in mechanical ones (Gravouil et al. 2002).

In our case, the level set method is used to represent the flow discontinuity generated by the presence of the IF between the TL and the FL. One of the advantages of this approach is that the model and mesh generation are incredibly simplified. Such simplification comes from the fact that the TL and FL are treated as a unique volume of fluid, disregarding the presence of the intimal flap, which is treated in a completely independent manner during the entire preprocess stage. This makes it possible to set up and test as many IF configurations as needed by only updating the IF geometry, without even remeshing the volume TL and FL domain. This feature is particularly interesting for the decision making before surgery since it makes possible to easily set up new IF configurations to assess their affectation to the blood flow.

The level set approach is also useful to get rid of the mesh update problems when the problem is solved considering the movement of the IF. Unlike in the FSI case, in which the aortic walls movement is a consequence of the fluid flow, in this case, the objective is to obtain the fluid flow but considering a known IF movement, which can be easily obtained by using medical imaging techniques. Taking into account the uncertainties associated with the IF thickness and mechanical behavior, this becomes a feasible robust alternative to the fully coupled FSI simulation of the AD.

Unfortunately, all the previous advantages come at the price of introducing some extra complexities that are not present in the common body-fitted approaches. On the one hand, it is required to use a robust auxiliary algorithm (Baumgärtner et al. 2018) to compute the level set function in accordance with the IF position. Besides, although the level set a robust and always defined operation, some details of the original geometry (e.g., sharp edges or corners) might be lost when computing its level set approximation.

With regard to the continuity of the level set function, it is possible to distinguish between two types of level set functions depending on the nature of the embedded body. If the geometry to be analyzed has a closed internal volume, a continuous level set function is commonly employed, although it is possible to use a discontinuous one. On the contrary, the bodies without internal volume, such as the IF, can only be represented by a discontinuous level set (Fig. 1). This means that in these cases the level set function is computed element by element, which implies that the same node can have different sign and values depending on the element considered. A much more detailed discussion about the continuity of the level set can be found in Zorrilla et al. (2019).

Once the embedded body (in this case the IF) is represented by a level set function, it is needed to impose proper boundary conditions over it. According to the nature of such boundary condition imposition, we can roughly divide the unfitted mesh methods in two families: immersed and

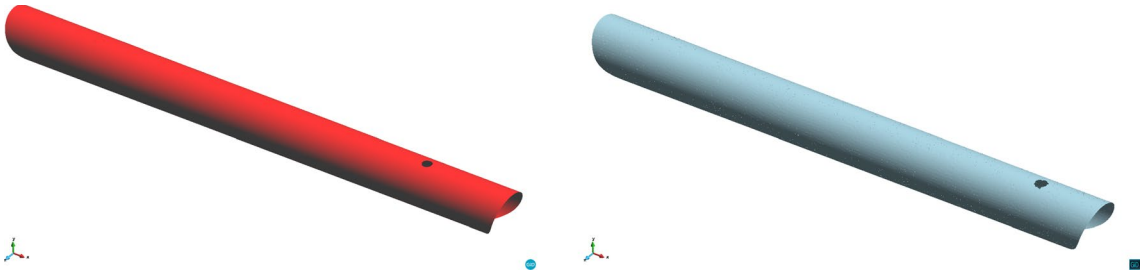

(a) Origin geometry **(b)** Level set intersections

Fig. 1 Intimal flap level set function representation

embedded mesh methods. Since the distinction between these two typologies of methods appears to be blurred in the literature, from now on, we will denote as immersed those formulations that use the nodes in the interior of the level set to impose the analyzed body movement. On the contrary, we denote as embedded those formulations that impose the boundary condition by using a variational (weak) technique over the zero isosurface of the level set. Considering that these works aim to represent the IF as a zero-thickness body, it is only possible to impose the boundary condition by using an embedded mesh method. The technique used for such boundary condition imposition is detailed in Sect. 2.3.

In the following subsections, we present the governing equations of the fluid dynamics problem as well as the level set boundary condition imposition technique.

2.2 Governing equations

The governing equations of the fluid dynamics problem are the conservation of linear momentum and the conservation of mass. In an Eulerian reference framework, these equations are

$$\rho\frac{\partial \mathbf{v}}{\partial t} + \rho(\mathbf{v}\cdot\boldsymbol{\nabla})\mathbf{v} - \boldsymbol{\nabla}\cdot\boldsymbol{\sigma} = \mathbf{f}_{\text{ext}} \tag{1a}$$

$$\frac{D\rho}{Dt} + \rho\boldsymbol{\nabla}\cdot\mathbf{v} = 0 \tag{1b}$$

where $\mathbf{v}$ is the velocity, $\mathbf{f}_{\text{ext}}$ is an external volume force (e.g., gravity) and ρ is the density. $\boldsymbol{\sigma}$ denote the Cauchy stress tensor which is computed as $\boldsymbol{\sigma} = -p\mathbf{I} + \mathbb{C} : \boldsymbol{\nabla}^{\text{s}}\mathbf{v}$, where p is the pressure, $\boldsymbol{\nabla}^{\text{s}}$ the symmetric gradient operator and $\mathbb{C}$ the constitutive tensor describing the viscous (shear) behavior.

Taking into account that the perfusion liquid used in the in vitro experiments reproduced in this work has similar properties to the water ones, we decided to model it as a viscous Newtonian fluid. Hence, the viscous constitutive tensor $\mathbb{C}$ in Eq. 1a can be substituted by the Newtonian one. The Newtonian constitutive tensor only depends on the dynamic viscosity μ and can be expressed in Voigt notation as the second-order tensor

$$\mathbb{C} = \begin{bmatrix} \frac{4\mu}{3} & -\frac{2\mu}{3} & -\frac{2\mu}{3} & 0 & 0 & 0 \\ -\frac{2\mu}{3} & \frac{4\mu}{3} & -\frac{2\mu}{3} & 0 & 0 & 0 \\ -\frac{2\mu}{3} & -\frac{2\mu}{3} & \frac{4\mu}{3} & 0 & 0 & 0 \\ 0 & 0 & 0 & \mu & 0 & 0 \\ 0 & 0 & 0 & 0 & \mu & 0 \\ 0 & 0 & 0 & 0 & 0 & \mu \end{bmatrix} \tag{2}$$

By substituting the previous definition of $\boldsymbol{\sigma}$ into the linear momentum conservation equation (Eq. 1a), it yields the well-known viscous Navier–Stokes equations

$$\rho\frac{\partial \mathbf{v}}{\partial t} + \rho(\mathbf{v}\cdot\boldsymbol{\nabla})\mathbf{v} - \boldsymbol{\nabla}\cdot(\mathbb{C} : \boldsymbol{\nabla}^{\text{s}}\mathbf{v}) + \boldsymbol{\nabla}p = \mathbf{f}_{\text{ext}} \tag{3a}$$

$$\frac{D\rho}{Dt} + \rho\boldsymbol{\nabla}\cdot\mathbf{v} = 0 \tag{3b}$$

For purely incompressible fluids, it is commonly assumed that the density time derivative $D\rho/Dt$ in Eq. 1b is zero, leading to the conventional viscous incompressible Navier–Stokes equation. This assumption is however not taken into account in here. Instead, we consider the simplified state equation $p = \rho c^2$, leading to the so-called viscous pseudo-compressible Navier–Stokes equations. This simplified equation of state relates the pressure with the density through the fluid speed of sound c. The purpose of adding this pseudo-compressibility is to tackle those cases in which isolated fluid cavities with no Neumann boundary condition appear. The apparition of such ill-defined cavities is commonly related either to dirty input skin geometries or to the movement of the embedded skin. If we further assume that the density fluctuations are negligible, the final form of the governing equations reads

$$\rho\frac{\partial \mathbf{v}}{\partial t} + \rho(\mathbf{v}\cdot\boldsymbol{\nabla})\mathbf{v} - \boldsymbol{\nabla}\cdot(\mathbb{C} : \boldsymbol{\nabla}^{s}\mathbf{v}) + \boldsymbol{\nabla}p = \mathbf{f}_{\text{ext}} \tag{4a}$$

$$\frac{1}{\rho c^2}\frac{\partial p}{\partial t} + \boldsymbol{\nabla}\cdot\mathbf{v} = 0 \tag{4b}$$

In all the cases presented in this work, we set the speed of sound c to 10^{12} m/s. This implies that the term $1/\rho c$ in Eq. 4b is reduced beyond the machine precision (10^{-16}), recovering thus the fully incompressible form of the Navier–Stokes equations. This is intentionally done since no isolated fluid cavities are expected due to the simplicity and steady nature of the level set function that represents the IF. However, it is due mentioning that this term might play an important role as soon as the problem is extended to consider the movement of the IF.

2.3 Modified finite element formulation and embedded imposition

Once the immersed body (IF) is represented by the level set function, proper boundary conditions need to be imposed over it. To that purpose, we rely on the use of a modified finite element (FE) space together with a Nitsche-based general Navier imposition.

On the one hand, we substitute the standard FE space by an alternative discontinuous one in those elements intersected by the level set. Such alternative space (henceforth named Ausas FE space after the name of the original author) was firstly proposed in Ausas et al. (2010). The main feature of the Ausas FE space is the capability to represent discontinuities inside an element. This makes it possible to capture the velocity and pressure fields discontinuities that arise between the TL and the FL due to the presence of the IF. Unfortunately, such capability comes at the price of having worse interpolation properties than the common FE space. Despite this limitation, the capability of the Ausas FE space to solve viscous incompressible fluid problems, ranging from the low to the high Reynolds (Re) scenario, is proved in Zorrilla et al. (2019).

On the other hand, a Robin-type general Navier condition (Eq. 5) is imposed over the level set intersections by using a Nitsche-based technique as it is described in Winter et al. (2018). The general Navier condition is composed by a Dirichlet no penetration condition in the normal direction to the level set zero isosurface (Eq. 5a) and a Robin condition to impose a shear force in the tangential direction to the level set zero isosurface (Eq. 5b). The normal and tangential contributions of the general Navier condition can be split in two equations as

$$(\mathbf{v}-\bar{\mathbf{v}})\mathbf{P}^{n} = \mathbf{0} \tag{5a}$$

$$\left(\varepsilon\left(\left[\mathbb{C} : (\boldsymbol{\nabla}^{s}\mathbf{v})\right]\cdot\mathbf{n} - \mathbf{h}\right) + \mu(\mathbf{v}-\bar{\mathbf{v}})\right)\mathbf{P}^{t} = \mathbf{0} \tag{5b}$$

where $\bar{\mathbf{v}}$ is the immersed body (IF) velocity, $\mathbf{n}$ is the unit normal vector to the level set and $\mathbf{h}$ an imposed shear traction. $\mathbf{P}^{n}$ and $\mathbf{P}^{t}$ are the normal and tangential projection operators obtained as $\mathbf{P}^{n} = \mathbf{n}\otimes\mathbf{n}$ and $\mathbf{P}^{t} = \mathbf{I} - \mathbf{n}\otimes\mathbf{n}$. ε is the so-called slip length, which regulates the tangential behavior of the boundary condition. Therefore, the general Navier condition behaves as a slip condition (no tangential velocity constraint) as $\varepsilon \to \infty$, while it approximates to a stick condition (null tangential velocity) as $\varepsilon \to 0$.

More details on the implementation, convergence and stability analysis of the general Navier condition and the Nitsche constraint can be found in Winter et al. (2018).

3 Experiment: aortic dissection model

3.1 Geometry

As one of the main objectives of this work is to reproduce the in vitro experiments in Rudenick et al. (2013), the phantom models used in this work are taken as reference geometry for the present study. Far from being patient-specific AD cases, these phantom models consist in a simplified geometry made of silicon and latex connected to a closed circuit that pumped water into it to emulate the AD blood flow. The geometry of these AD phantom models is simplified to two straight and constant diameter tubes (the aortic arch is not taken into account) whose thickness is assumed to be infinitesimal. The IF is also considered to be an infinitesimal thin wall (Figs. 2, 3). The two straight tubes axes are aligned with the X-axis of the global coordinates system, whose origin is located in the center of the inlet face.

As was originally done in Rudenick et al. (2013), we distinguish the different study cases according to the proximal and distal tears diameter. Table 1 collects each one of the

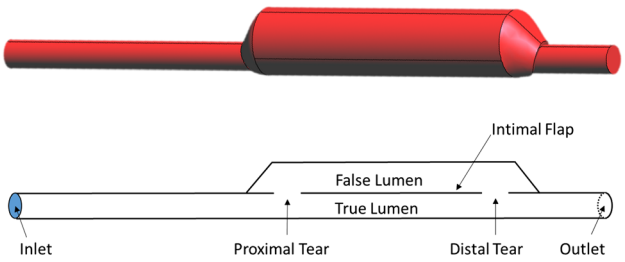

Fig. 2 Three-dimensional geometry model of the type B aortic dissection and longitudinal cross-sectional plane. The diameter of the tube representing the TL is 16 mm, while its length is 390 mm. On the other hand, the diameter of the tube representing the FL is 37 mm. The dissection length is 160 mm, and it is set up by aligning the inferior parts of the TL and FL tubes. The proximal and distal tears were simulated by creating two holes, which diameters range from 0 to 10 mm, in the FL tube. The center of the proximal and distal tears is 177.5 mm and 322.5 mm from the inlet

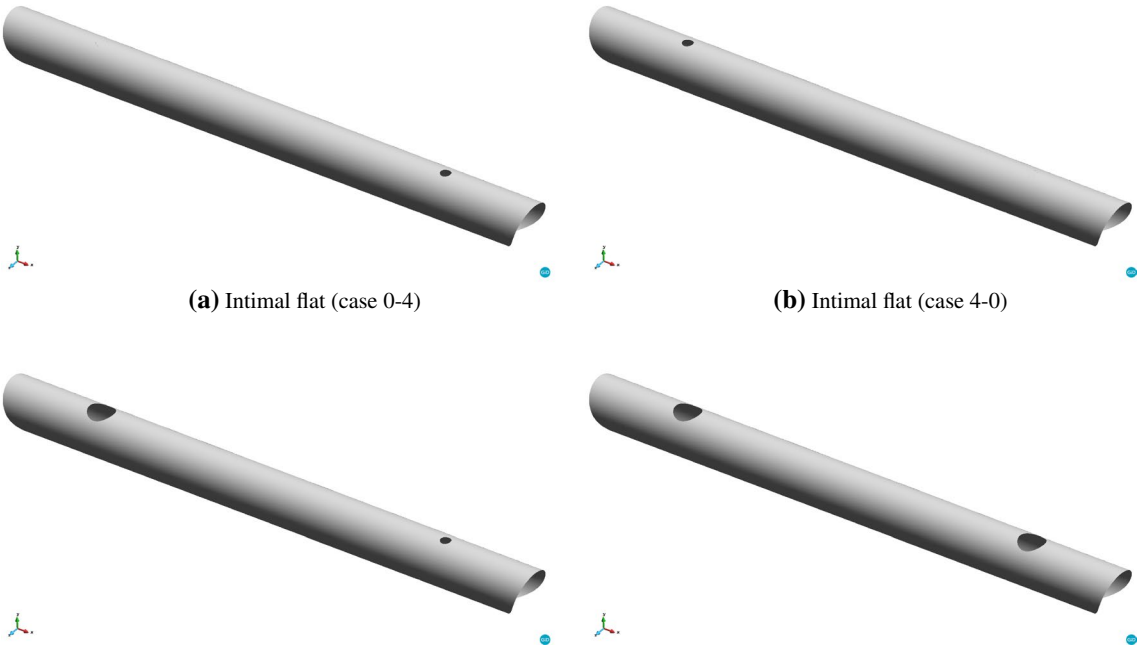

(a) Intimal flat (case 0-4)

(b) Intimal flat (case 4-0)

(c) Intimal flat (case 10-4)

(d) Intimal flat (case 10-10)

Fig. 3 Intimal flat geometries for the four validation cases studied. These are the input geometries for the computation of the level set function used in the resolution of the embedded CFD problems

study cases together with their proximal and distal tears diameter. Henceforth, we will refer to the cases as Case *proximal tear diameter—distal tear diameter* (e.g., Case 0–4 stands for no proximal tear and 4 mm distal tear diameter).

It is worth mentioning that thanks to the embedded approach used in this work the geometry and the mesh generation are significantly simplified compared with the common body-fitted approach. The key advantage is that a unique volume mesh needs to be generated for all the cases to be studied. This volume mesh is built from the outer skin, which at the same time is conformed by the aggregation of the inlet and outlet tubes skin together with the enlarged tube one representing the FL. Once the volume mesh is generated, each simulation case can be defined by simply dropping the surface mesh representing its IF into the volume mesh and computing its level set function, which is obtained from the intersections between the AD volume mesh and IF surface one.

We would like to stress again the potential of the presented method to be exploited when multiple IF configurations need to be efficiently tested (e.g., decision making before surgery). We also highlight that the complex preprocess operations commonly associated with the CFD simulation of volumeless geometries (e.g., edge and surface duplication) are completely avoided as the volume mesh is meshed with no regard of the immersed volumeless structures.

3.2 Material properties

The perfusion liquid used in the original in vitro experiments is water at room temperature, which is less viscous than blood. According to the original authors, no noticeable differences in the velocity values can be observed if they are compared with the ones obtained by using a glycerin-water solution, whose viscosity and density are similar to blood ones (Rudenick et al. 2013). Taking this into consideration, we decided to set the fluid material properties to be similar to the blood ones. Therefore, the density is set to 1050 kg/m^3 , while the dynamic viscosity is set to $3.5 \cdot 10^{-3}$ kg/ms.

3.3 Boundary conditions

The boundary conditions are selected to emulate each one of the reference in vitro experiments in Rudenick et al. (2013), meaning that each AD scenario has its own velocity and pressure waveform. On the one hand, the fluid flow generated by the pumping system of the in vitro experiments is reproduced by setting the inlet velocity function $v_M(t)$. On the other hand, the outlet pressure waveform $p_M(t)$ is taken directly from experiments measurements and imposed in the outlet region. Both inlet velocity function and outlet pressure waveform are directly extracted from the reference in vitro experiments datasets.

The above-mentioned inlet velocity function v_M is applied to the inlet surface as a parabolic profile in such a way that the reference in vitro experiments flow rate is kept. Thus, the velocity in each one of the inlet nodes can be computed as

$$\mathbf{v}^{\text{in}}(r,t) = 2.0 v_M(t)\left(1 - \frac{r}{R^2}\right)\mathbf{n}_{\text{in}} \tag{6}$$

where r denotes the in-plane distance from the inlet center point to the considered inlet node, R the radius of the inlet surface, whose value is 0.008 m, and $\mathbf{n}_{\text{in}}$ the vector normal to the inlet surface pointing in the inward direction.

The outlet pressure is fixed to the $p_M(t)$ waveform values. To fulfill the force equilibrium in the outlet region, it is also required to set the external traction that corresponds to the $p_M(t)$ values. This can be computed as $\mathbf{t} = p_M(t)\mathbf{n}$.

We consider that the rest of boundary surfaces that conform the AD computational volume have a stick (no-slip) behavior, something that turns into a null velocity constraint. The same no-slip behavior is assumed in the embedded IF. Therefore, the slip length (ε) in Eq. 5b is set to 0 in all the cases.

3.4 Simulation settings

The problem is discretized in time using a second-order backward differentiation formula (BDF2). The available data sets in Rudenick et al. (2013) comprehend a period of 0.88 s, which is enough to represent a normal hemodynamic cycle of the human aorta: the peak pressure (reached at 0.25 s) and a biphasic diastolic period. Based on this, we set the total simulation time to 0.8 s, which is also enough to represent all the aortic cycle features, and the time step of $2.5 \cdot 10^{-3}$ s.

The use of the BDF2 formula results in an implicit time discretization, which preferred because of its well-known stability properties. However, such enhanced stability comes at the price of requiring to solve a nonlinear system of equations at each time step. This is achieved by using a Newton–Raphson strategy, with linearized convective velocity, in combination with a mixed pressure and velocity convergence criterion. The relative and absolute tolerances are 10^{-4} and 10^{-6} for both the pressure and velocity residuals.

As it is highlighted above, one of the remarkable features of the presented approach is that the same background mesh is always used with no regard of the analyzed IF configuration. Therefore, a unique volume mesh conformed by approximately 7M linear tetrahedrons is used in all the presented cases. All the simulations are run in our internal high-performance computing (HPC) facilities (Acuario cluster) using a parallel distributed memory environment (MPI parallelism). For all the cases, we take four nodes with 16 Intel Xeon E5-2670 processors and 64 GB of memory. This amounts a total of 64 processors and 256 GB of memory. The elapsed wall clock time in all cases is less than 12 h.

4 Results

4.1 Validation

This section presents the results of the AD scenarios described in the previous section. In all the cases, we compare the results obtained by using the presented embedded approach with the results obtained from the reference in vitro experiments in Rudenick et al. (2013). The AD cases with a single tear (case 4–0 and case 0–4) are also validated with the CFD simulation results in Soudah et al. (2015). The results validation mainly consists in comparing the pressure time evolution in the four control points stated in Rudenick et al. (2013) and Soudah et al. (2015). The coordinates of these pressure measurement points are collected in Table 2.

4.1.1 1 Tear cases

For assessing the effect of the tears number upon the fluid flow, next we consider a configuration with a unique tear: Case 4–0 (A) and Case 0–4 (B). In both cases, the proximal or distal tear has a diameter of 4 mm. The inlet and outlet boundary conditions are identical to the ones used in the in vitro experiments (Fig. 4). Before any further discussion, it is interesting to remark that the in vitro pressure measurements were done using retrograde catheterization. This could have induced a partial obstruction of the tears, reducing thus their effective diameter, something that could have altered FL pressure measurements (especially in the small tear cases). Furthermore, it is important to mention that in these particular cases, the experimental data measurements in the FL region appear to have been incorrectly taken (Fig. 3a, b). Taking this into consideration, we decided to also use the numerical results in Soudah et al. (2015) to properly validate these AD scenarios.

Figure 5 shows the pressure evolution at the reference points for case 4–0. Figure 6 presents the same results for case 0–4. As it can be observed, pressures at the TL (proximal and distal locations) are nearly identical in both cases. For both case 4–0 and case 0–4, a similar pressure waveform can be observed. However, the peak pressure reported in Soudah et al. (2015) is higher than the result obtained in this work. Considering that the presented results better fit the experimental ones, we believe that these differences are associated with the different discretization levels (1.5 M elements vs 7 M) as well as to the IF geometry modeling. Moreover, in this work, the IF is considered to have an infinitesimal thickness, while in Soudah et al. (2015), the thickness is 2 mm.

It is also interesting to remark that single-tear models show near zero FL flow (Figs. 7, 8). In both cases, there is

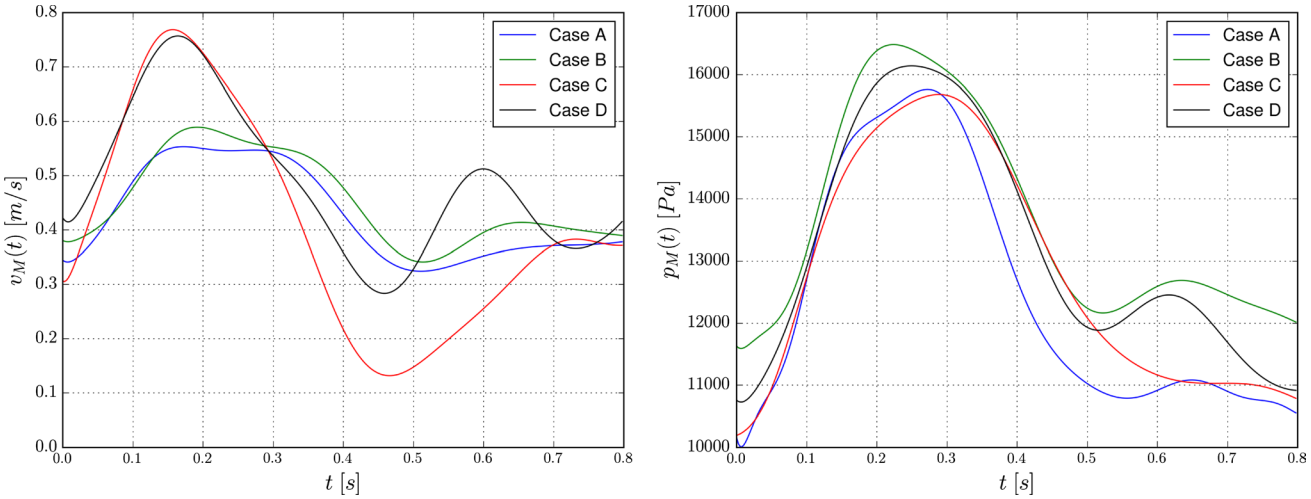

(a) Inlet velocity (m/s)

(b) Outlet pressure (Pa)

Fig. 4 Inlet velocity and outlet pressure waveform used in the four AD validation cases. On the left side, the inlet velocity time evolution is shown. On the right one, the outlet pressure time evolution is shown. These data have been extracted from reference in vitro experiments in Rudenick et al. (2013)

Table 1 Cases studied

Case	Case Id.	Proximal tear		Distal tear	
		Diameter (mm)	Coordinates (mm)	Diameter (mm)	Coordinates (mm)
Case 4–0	A	4	(177.5, 9.0, 0.0)	0	(No tear)
Case 0–4	B	0	(No tear)	4	(320.5, 9.0, 0.0)
Case 10–4	C	10	(177.5, 9.0, 0.0)	4	(320.5, 9.0, 0.0)
Case 10–10	D	10	(177.5, 9.0, 0.0)	10	(320.5, 9.0, 0.0)

Table 2 Control points coordinates

	Proximal tear		Distal tear	
	True lumen	False lumen	True lumen	False lumen)
Coordinates (mm)	(177.5, 0.0, 0.0)	(177.5, 17.5, 0.0)	(320.5, 0.0, 0.0)	(320.5, 17.5, 0.0)

only a small jet entering into the FL, while a slightly wider jet in the opposite direction enters into the TL during the peak systole. At peak diastole, it can be observed that the flow behaves in the opposite manner. In these cases, we observe large velocity decreases in the FL, leading to an negligible flow rate. This low fluid velocity in the FL favors the thrombus formation in single-tear AD as it is observed in the daily clinical routines.

4.1.2 2 Tears cases

In this section, we analyze the double (proximal and distal) tear configuration scenarios: Case 10–4 (C) and Case 10–10 (D). Case 10–4 involves a proximal tear of 10 mm and a distal tear of 4 mm, while Case 10–10 involves two tears of equal diameter (10 mm). The inlet and outlet boundary conditions are identical to the ones used in the reference in vitro experiments (Fig. 4).

Again, we compare the waveform and values of the pressure recorded in the different control points with the in vitro experiments reference ones (Figs. 9, 10). With regard to the pressure waveforms, bare differences can be observed between the numerical and experimental approaches. Concerning the pressure values, specially the systolic peak ones, the TL and FL obtained values are apparently equal to the reference ones in the Case 10–10. However, it can be observed that the TL and FL systolic peak values in the Case 10–4 are slightly lower than the ones reported in Rudenick et al. (2013), being the maximum error around the 5% (FL proximal tear control point). These differences are possibly

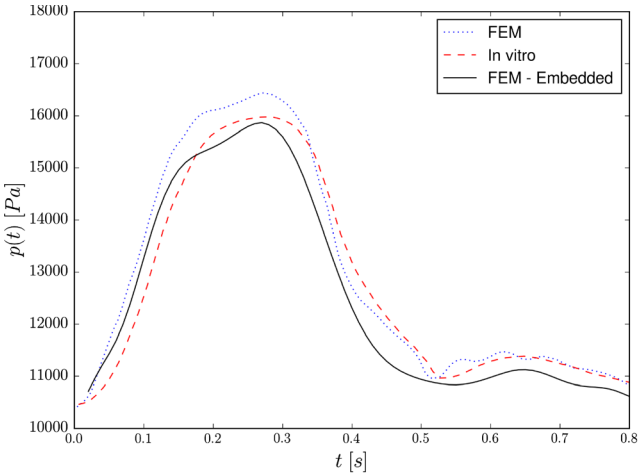

(a) Case A - TL proximal pressure

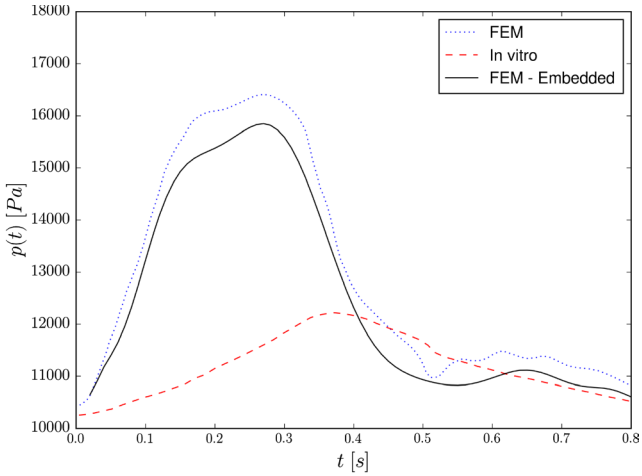

(b) Case A - FL proximal pressure

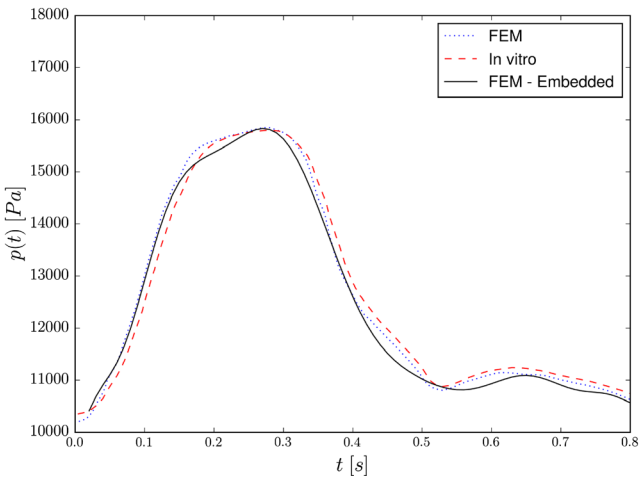

(c) Case A - TL distal pressure

Fig. 5 Case A. Pressure evolution at various locations. Comparison with the results in Rudenick et al. (2013) and Soudah et al. (2015)

associated with the fact that our model considers the IF as a rigid body, while it was flexible in the original in vitro experiments. A similar trend in the results can be also observed in Soudah et al. (2015) and Ben Ahmed et al. (2016).

The equal pressure evolution in the control points proves that the presence of a distal tear prevents large pressure gradients between FL and TL to occur. We also observe that large distal tears increase the pressure in the FL, leading to a diminution in the pressure gradient within the AD. It is also interesting to comment that the presence of two tears in the IF yields a flow recirculation in the FL, which is around a 20% higher in the Case 10–10 if we compare to the small distal tear Case 10–4. Therefore, during the systole phase, the flow enters from the TL to the FL through the proximal tear, while it leaves the AD through the distal one. Conversely, the opposite behavior occurs during the diastole phase. A natural consequence of such recirculation is that the flow in the FL becomes more chaotic, leading thus to the generation of some observable vorticity effects. Such increment in the vorticity is known to increase the wall shear stress, which is directly related to the redissection, or even rupture, risk.

4.2 Surgical application: reentry tear aortic fenestration

In this section, we want to show the capability of the presented methodology to easily generate new computational models to study the AD surgical fenestration technique. Surgical aortic fenestration represents an effective alternative for the treatment of ischemic complications of the AD, particularly in those patients with no aortic dilatation. This surgical procedure is less invasive than the thoracic endovascular aortic repair (TEVAR) (Nauta et al. 2017) as

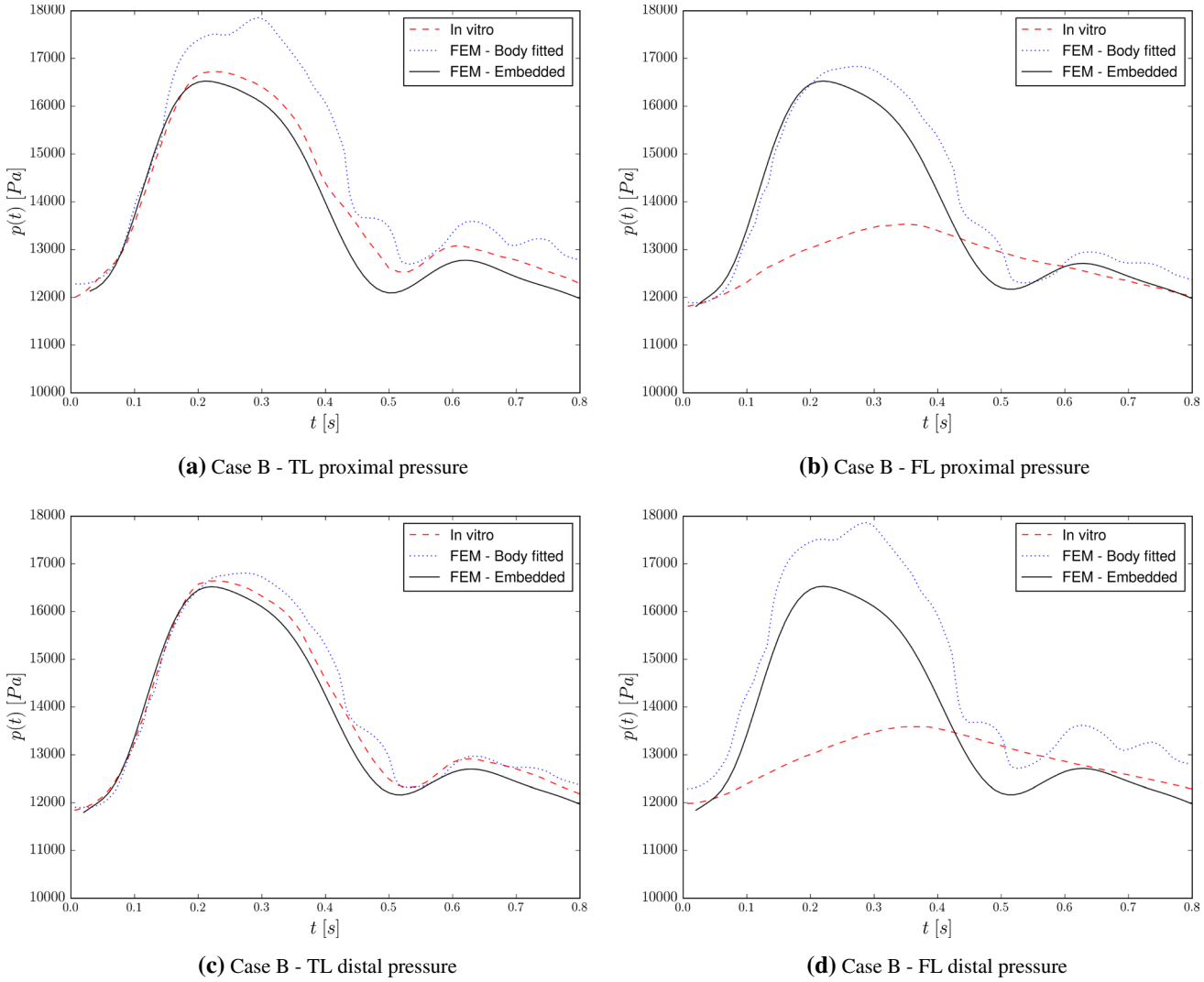

(a) Case B - TL proximal pressure

(b) Case B - FL proximal pressure

(c) Case B - TL distal pressure

(d) Case B - FL distal pressure

Fig. 6 Case B. Pressure evolution at various locations. Comparison with the results in Rudenick et al. (2013) and Soudah et al. (2015)

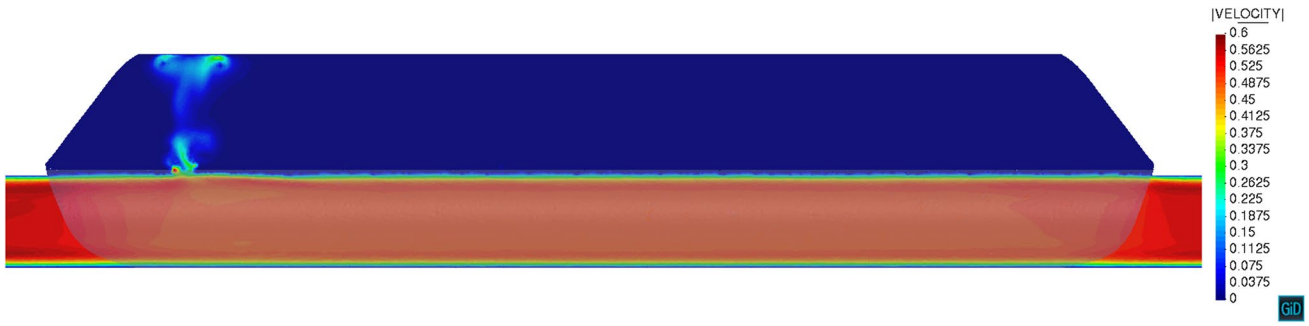

Fig. 7 Case A. Velocity cross section at $t = 0.09$ s. IF level set representation shadowed over the cross section

it only requires a puncture of the IF from the TL to the FL using a needle. This technique corrects the malperfusion at the suprarenal or infrarenal levels by creating a single aortic lumen intended to restore the organ flow. The aortic fenestration is also used to decompress the hypertensive FL thanks to the creation of the new reentry tear in the distal part of the IF (Hartnell and Gates 2005; Canchi et al. 2018). Considering that the mortality rate of patients without

Fig. 8 Case B. Velocity cross section at $t = 0.03$ s. IF level set representation shadowed over the cross section

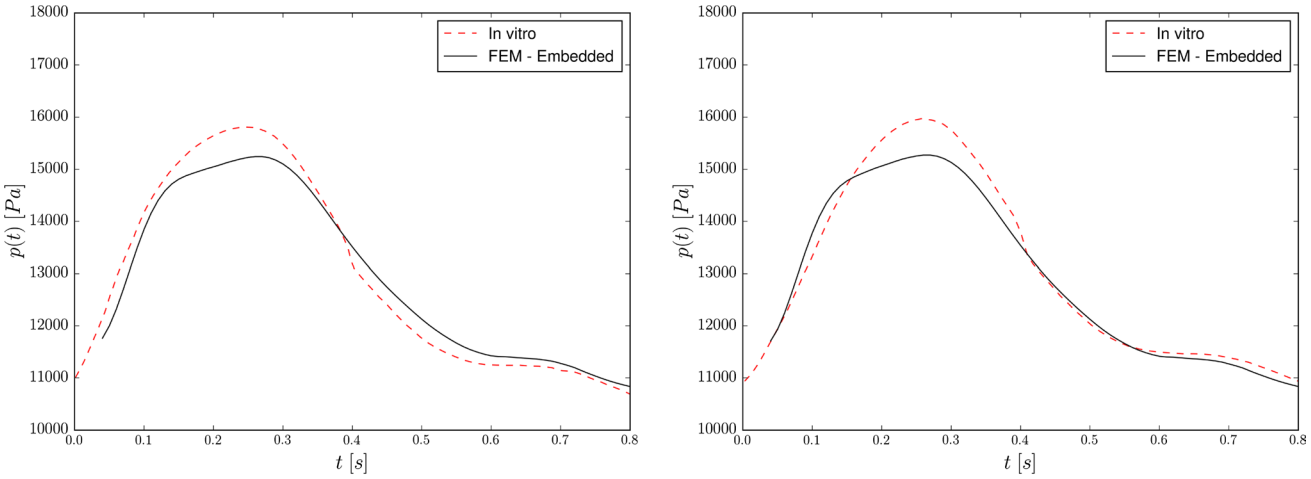

(a) Case C - TL proximal pressure

(b) Case C - FL proximal pressure

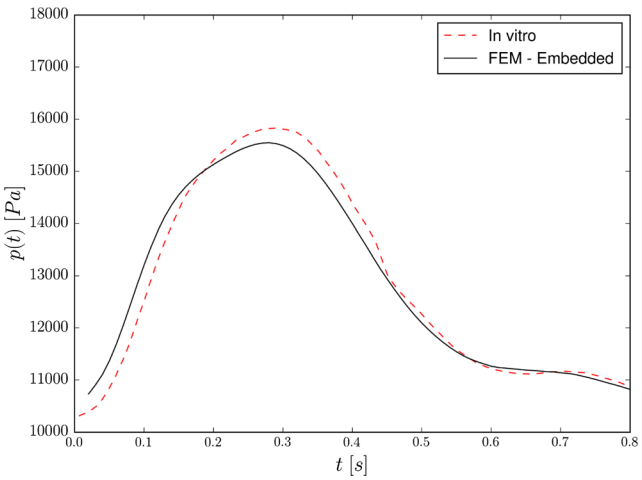

(c) Case C - TL distal pressure

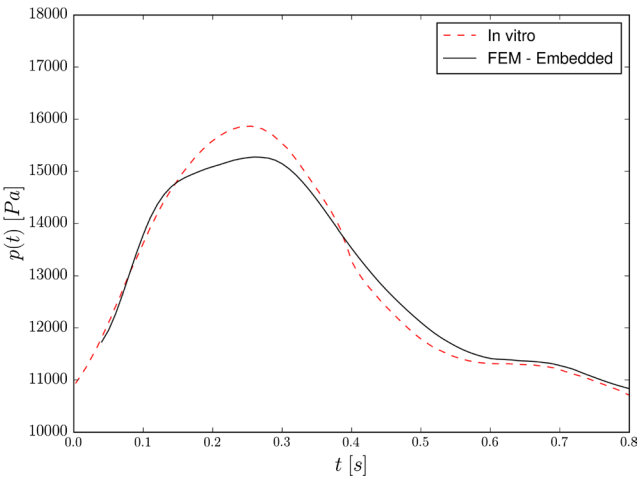

(d) Case C - FL distal pressure

Fig. 9 Case C. Pressure evolution at various locations. Comparison with the results in Rudenick et al. (2013)

fenestration is higher than the one in patients with exit or reentry tears, Tsai et al. (2008), evinces the importance of having noninvasive tools to a priori assess the consequences of the surgical fenestration before the clinical intervention.

We took case A as application case. Starting from the original IF geometry, we generate an artificial reentry tear in the midpoint of the IF top line (Table 3) to assess the

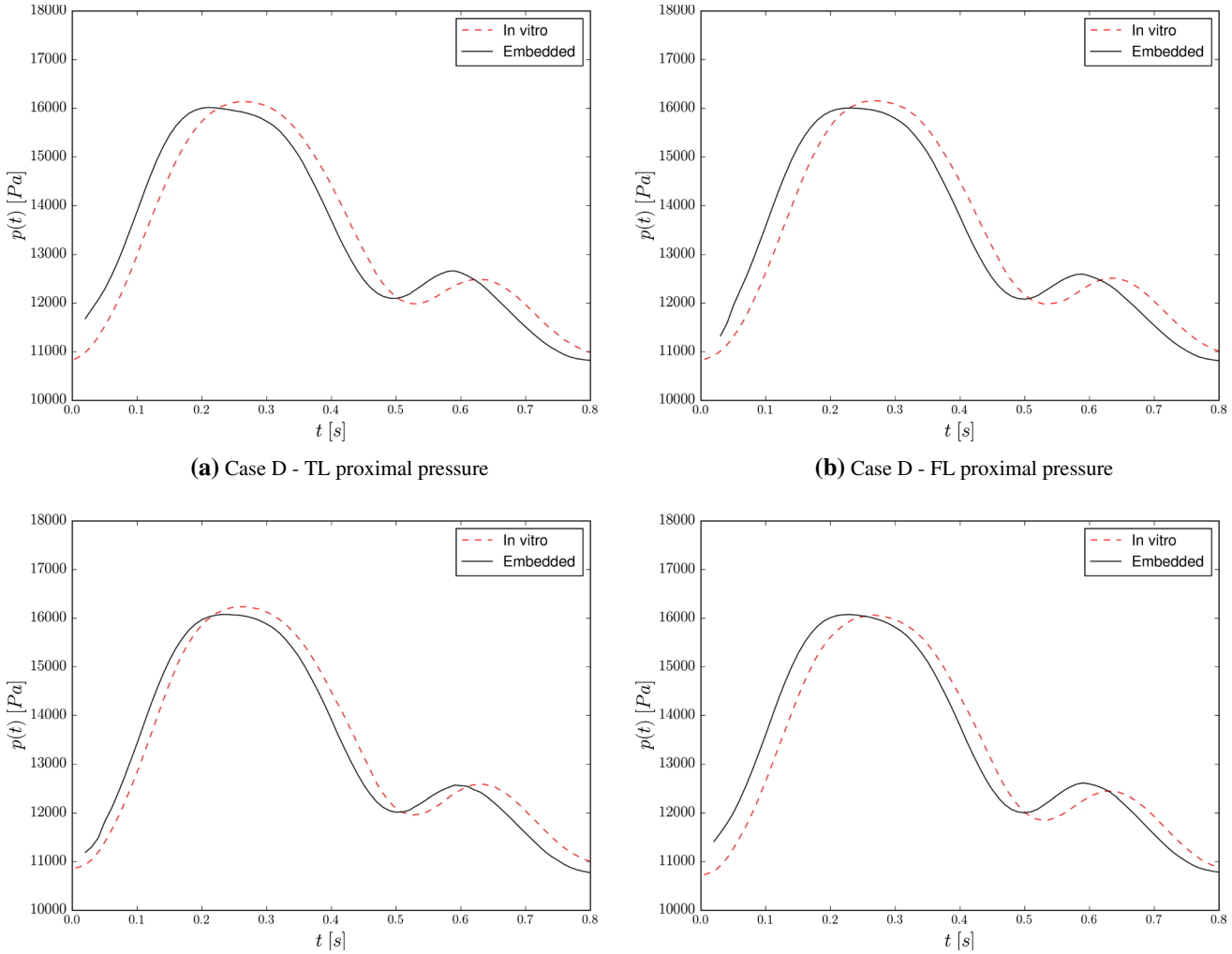

(a) Case D - TL proximal pressure

(b) Case D - FL proximal pressure

(c) Case D - TL distal pressure

(d) Case D - FL distal pressure

Fig. 10 Case D. Pressure evolution at various locations. Comparison with the results in Rudenick et al. (2013)

Table 3 Fenestration cases studied

Case	Case Id.	Proximal tear	Mid tear(s)	Distal tear
Case 4–10–0	A_F	(177.5, 9.0, 0.0)	(249.0, 9.0, 0.0)	(No tear)

affectation of the surgical fenestration to the velocity and pressure fields.

4.2.1 Embedded reentry tear generation

First of all, it is important to highlight that the creation of the new reentry tear is automatically done without any geometrical operation. The methodology implemented to create the new re-tear is described in algorithm 1. This algorithm only requires the user to introduce the radius (r^{fen}) and center ($\mathbf{x}_{\mathbf{c,fen}}$) of the new reentry tear. After the definition of these magnitudes, the routine flags the IF skin elements lying inside the fenestration radius. Once the marked elements are identified, they are deactivated to recompute the level set function with this new modified skin mesh. We would like to highlight again the simplicity of the methodology from the end-user perspective, as it avoids any preprocessing operation (including remeshing) thanks to the capabilities of the embedded approach. Besides, the presented approach has no limitation in the number of reentry tears, so could be possible to consider more than one.

ALGORITHM 1

Algorithm to place a fenestration tear in the intimal flap mesh.

```
r_fen                                              ▷ Fenestration radius
x_c,fen                                            ▷ Fenestration center point
fluid_mesh                                         ▷ Fluid mesh container
if_skin_mesh                                       ▷ Intimal flap mesh container

for if_skin_mesh.Elements() do
    x_c,elem = if_element.Center()                 ▷ Intimal flap element center
    dist = ||x_c,fen − x_c,elem||                  ▷ Distance from x_c,fen to x_c,elem
    if dist ≤ r_fen then                           ▷ Check if the current entity belongs to the fenestration
        if_element.Set(TO_ERASE)
    end if
end for

if_skin.RemoveElements(TO_ERASE)                   ▷ Remove the selected intimal flap entities
CalculateDiscontinuousDistance(fluid_mesh,if_skin_mesh)   ▷ Calculate the level set to the intimal flap mesh
```

4.2.2 Embedded surgical fenestration results

Figure 11 compares the results obtained after the surgical fenestration (case A_F) with the original ones with no fenestration (case A). Prior to any assessment, it is due mentioning that in this case, the results are not presented for the absolute pressure but for the pressure drop of the control points. Since we assume identical outlet pressure values in both cases (with and without fenestration), the pressure drop is computed as the pressure difference between the control points and the outlet.

Table 4 shows the maximum pressure differences at the proximal, mid (new reentry tear) and distal points for case A and A_F. Even though the surgical fenestration seems to barely affect the TL pressure evolution, Fig. 11 clearly shows that the surgical fenestration reduces the systole and diastole pressure peak values in the FL (difference between the TL and FL pressure values) (Fig. 12). Figure 12 also proves that the pressure difference between the TL and FL is almost negligible in the midpoint. Moreover, the pressure difference between the TL and FL decreases 120 Pa in the distal region of the AD. These results are in line with the medical protocols, which have traditionally promoted the use of surgical fenestration in one tear scenarios.

However, the creation of the distal reentry tear increases the flow rate in the FL (Fig. 13c). This artificially generated flow pattern complicates the generation of the thrombus in the AD. We also observe that the pressure difference grows in the proximal region. This is possibly due to the fact that the flow between the TL and FL increases, with the consequent increase in the energy local losses of the proximal tear. Clinical findings increasingly suggest, that patients with a partially thrombosed FL are at a higher risk of rupture (Tsai et al. 2007). Conversely, completely thrombosed FL have a better prognosis (Song et al. 2011). Indeed, it has been suggested that 'complete thrombosis of the residual FL might be a sign of aortic wall healing and remodeling' (Tsai et al. 2008). Therefore, we can conclude that the FL artificial flow pattern generated after the aortic fenestration is directly related to the thrombosis of FL (Yazdani et al. 2018).

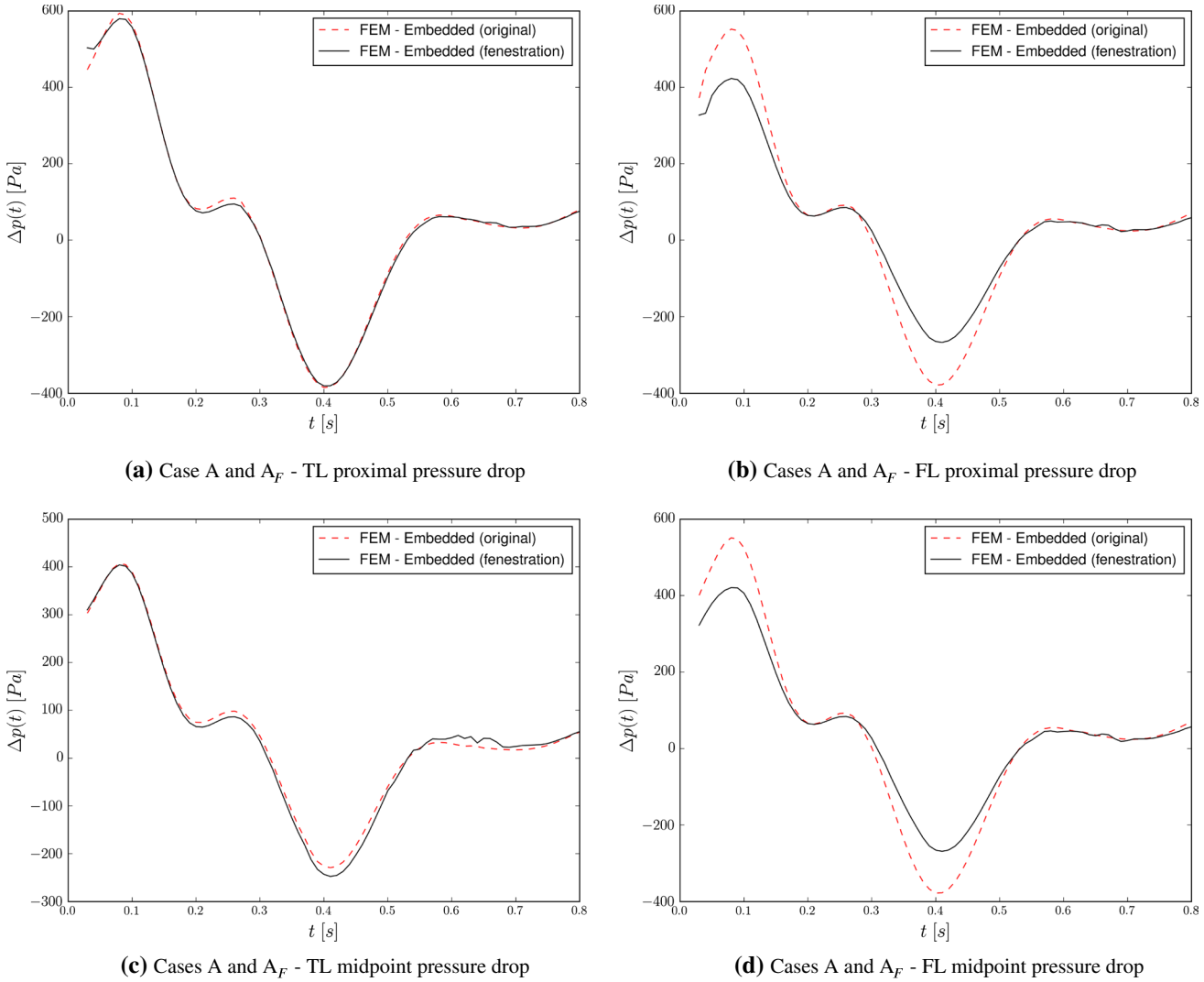

(a) Case A and A_F - TL proximal pressure drop

(b) Cases A and A_F - FL proximal pressure drop

(c) Cases A and A_F - TL midpoint pressure drop

(d) Cases A and A_F - FL midpoint pressure drop

Fig. 11 Case A_F. Pressure drop evolution at various locations. Comparison with Case A (before fenestration) pressure drop results

5 Conclusion

In this work, we propose a new numerical FE-based embedded technique to study the fluid flow in biomedical applications, in particular to AD scenarios. The FE embedded technique is developed and implemented by the authors in the Kratos Multiphysics framework (Dadvand et al. 2010). The presented method is validated by reproducing the in vitro experiment described in Rudenick et al. (2013). After the successful validation, and with the objective of showing the advantages of the proposed approach, we reproduced a surgical fenestration technique. The presented embedded technique makes it possible to easily modify the IF geometry without the necessity of modifying the volume mesh.

It is known that pressure differences between TL and FL may indicate conditions of AD growth (Tolenaar et al. 2013). Taking this into consideration, the validation is based on measuring the pressures in a set of control points in the TL and FL. After solving multiple cases, we dare say that the

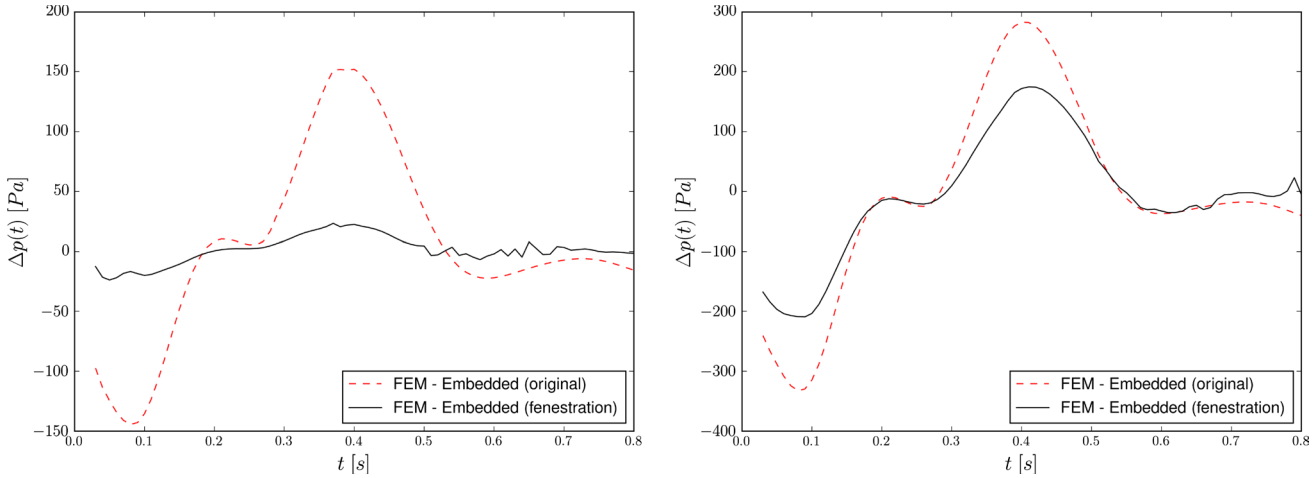

(a) Midpoint **(b)** Distal point

Fig. 12 Pressure difference between TL and FL. Positive values means higher pressure in TL, whereas a negative value means higher pressure in FL

presented methodology is capable to reliably represent the fluid flow inside an AD. We also notice that the maximum pressure peaks occur for the single-tear cases. This leads us to consider the introduction of a new reentry tear in the IF, mimicking a surgical fenestration intervention. Such new tear introduction yields a diminution in the TL and FL pressure difference as shown in Fig. 12. The comparison between the two tear cases (C and D) shows that a small distal tear reduces the pressure difference. On the contrary, large distal tears result in negligible pressure difference between the TL and FL. This observation confirms that a small tear size yields an insufficient reduction in the FL pressure. These results are in line with the conclusions in Berguer et al. (2015), which state that the pressure difference between the TL and the FL is inversely proportional to the cross-sectional area of the exit tear. It can be also observed that the tear jet becomes relevant only in those cases involving two tears (Figs. 14, 15). These fluid jets affect the FL wall and could eventually generate a high wall stress. Furthermore, these cases also show that a small distal tear induces a reduced jet impact in the proximal region of the FL (Fig. 14). A detailed analysis of the flow through the tears reveals that the jets are typically shifted in the direction of the flow (downstream).

We would also like to highlight that all the AD cases have been solved with a unique volume mesh. This is thanks to the capability of the method to represent the IF by using a discontinuous level set function. Note that the level set movement could eventually be considered by simply updating the level set function. This feature becomes crucial for the application of the presented approach in the biomedical field since it would make it possible to solve a FSI problem without any knowledge of the mechanical properties of the tissue, whether it is healthy or not (Alimohammadi et al. 2015; Chen et al. 2016). In this particular case, the movement of the IF can be obtained using 4D PC-MRI techniques (Liu et al. 2018; Sherrah et al. 2017; Soudah et al. 2011). 4D-PC-MRI techniques can provide the characteristic features of the flow in the entire aortic volume for any specific time window (Dillon-Murphy et al. 2016). For each time frame, the displacement of the IF could be recorded and used as a boundary condition in our method. As a second step, the mechanical properties of the IF could be eventually estimated by performing an inverse analysis after computing the pressure distribution in the TL and FL. Although the presented approach is already prepared to be used in combination with any imposed movement of the IF, there are still some complexities to be tackled. These are mainly related with the input data acquirement. Handling these data could be also a issue as it is required to do, store and manage the IF segmentation, together with the tear(s) location.

The capability of the model to easily create artificial tears is also proved. Then, it could be possible to use the presented technique to efficiently study the flow pattern in AD patients after stent-grafting repair. The location of the stent-graft into

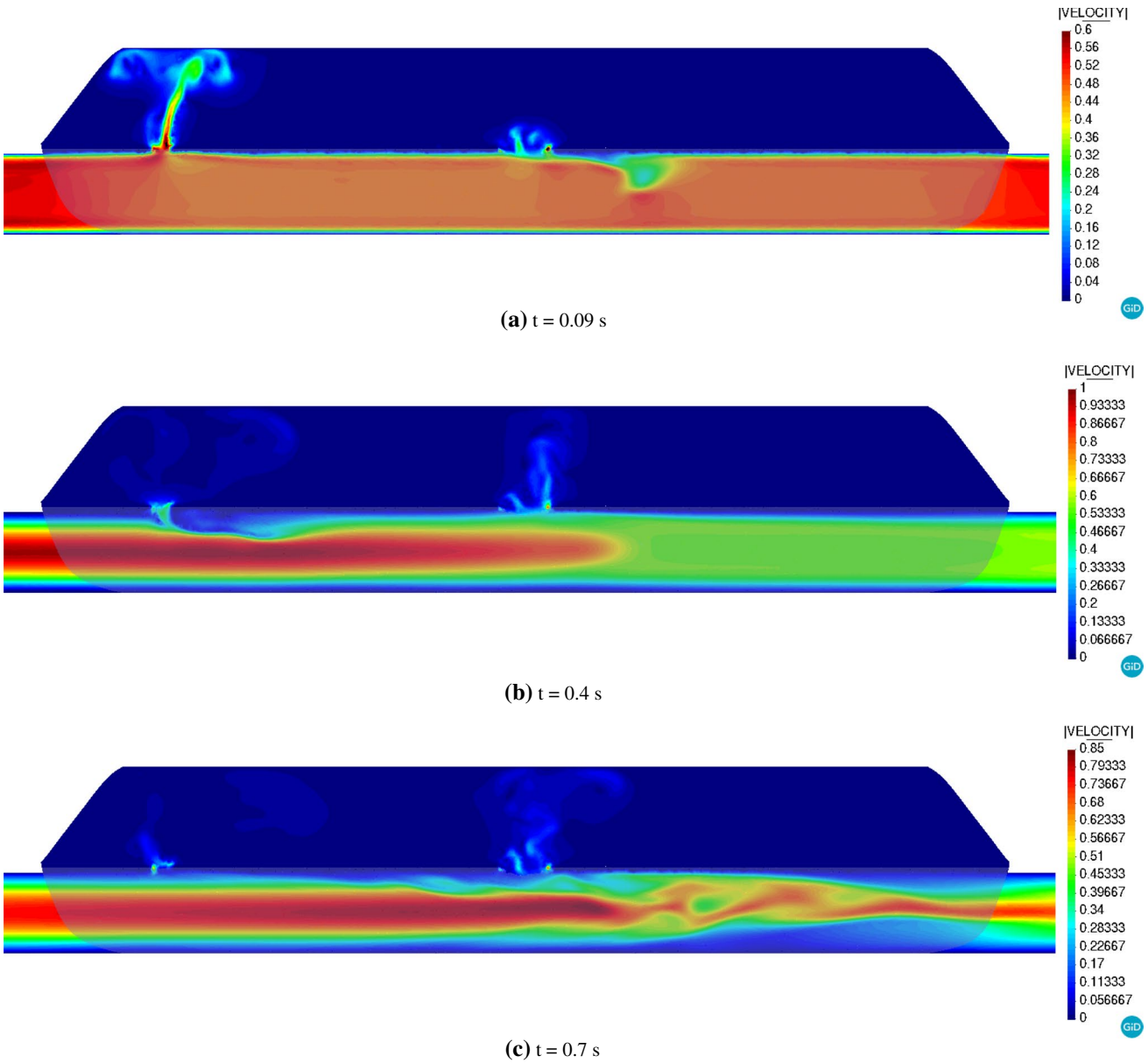

Fig. 13 Case A_F. Velocity cross section at different time steps. IF level set representation shadowed over the cross section

Table 4 Pressure difference between TL and FL control points. Positive values means higher pressure in TL, whereas a negative value means higher pressure in FL

Case	Pressure Difference (P_{TL}-P_{FL})		
	Proximal (Pa)	Mid (Pa)	Distal (Pa)
Case 4–0	41.246	152.021	− 332.684
Case 4–10–0	167.937	23.774	− 209.312

the AD volume can be described by a level set function to study the new flow pattern distribution.

Finally, we would like to remark that this work is conceived as a preliminary validation and proof of concept of a new research line that aims to exploit the capabilities of fixed mesh methods in the framework of biomedical applications. In the short term, we plan to apply our methodology to study patient-specific data coming from 4D-PC-MRI and to extend it to consider the movement of the IF.

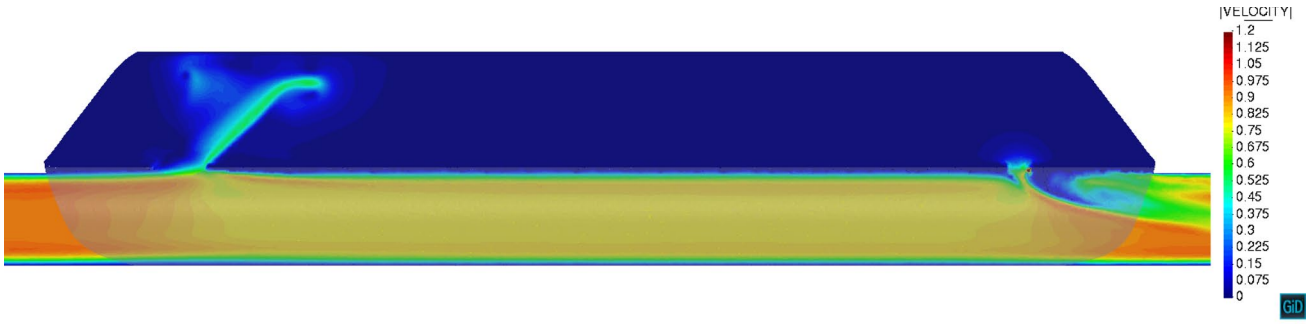

(a) t = 0.15 s

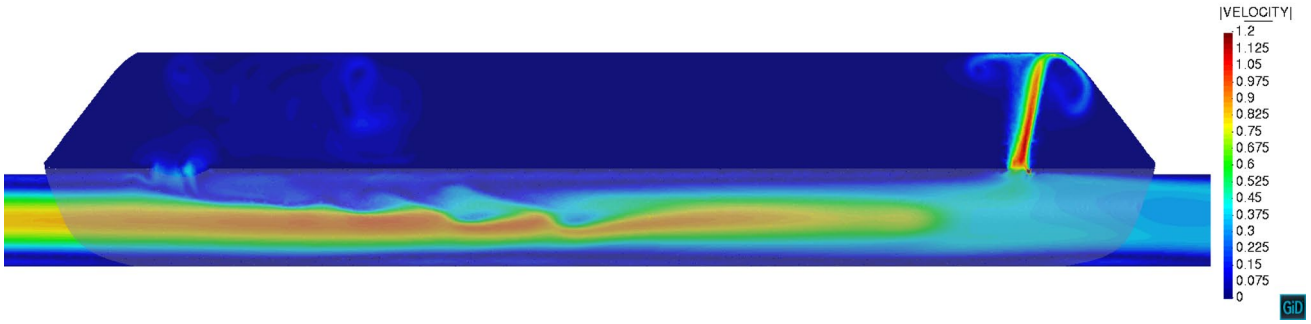

(b) t = 0.4 s

Fig. 14 Case C. Velocity cross section at different time steps. IF level set representation shadowed over the cross section

(a) t = 0.09 s

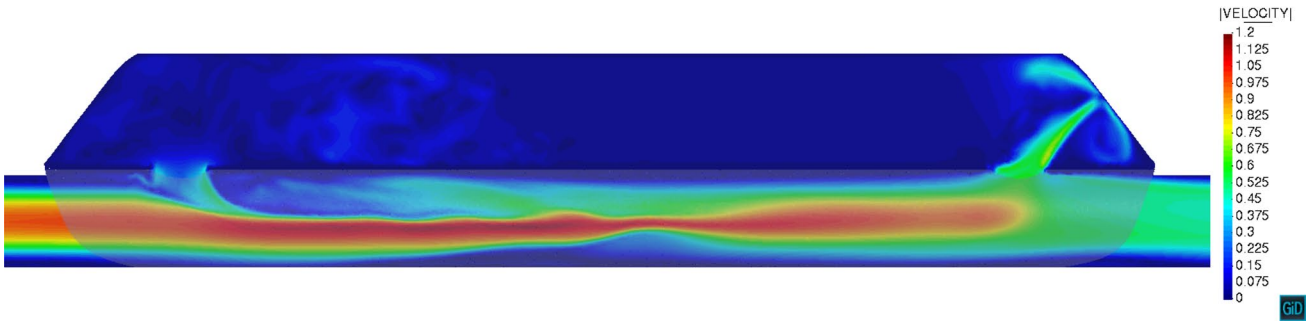

(b) t = 0.4 s

Fig. 15 Case D. Velocity cross section at different time steps. IF level set representation shadowed over the cross section

Acknowledgements This research has been partly supported by the European Commission (EC) through the Project ExaQUte (H2020-FETHPC-2016-2017-800898). Rubén Zorrilla gratefully acknowledges the support of the Spanish Government for his FPU Grant (FPU15/03796). Finally, the authors want to express their gratitude to Dr. Antonio J. Barros for his fruitful discussion about AD, Dr. Paula A. Rudenick and Dr. Bart H. Bijnens for providing the experimental data of the in vitro tests, as well as to the Spanish Research Network for Cardiac Computational Modeling (V-Heart-SN) for the interest expressed.

Author contributions Investigation was done by RZ, ES and RR. Model implementation was carried out by RZ. Geometrical modeling was done by ES. Data processing was carried out by RZ and ES. Validation was made by RZ and ES. Visualization was carried out by RZ and ES. Discussion was carried out by RZ, ES and RR. The paper was written by RZ, ES and RR.

Compliance with ethical standards

Conflict of interest The authors declare that they have no conflict of interest.

References

Alimohammadi M, Sherwood J, Karimpour M, Agu O, Balabani S, Díaz-Zuccarini V (2015) Aortic dissection simulation models for clinical support: fluid-structure interaction vs. rigid wall models. Biomed Eng Online 14(1):34

Ausas R, Sousa F, Buscaglia G (2010) An improved finite element space for discontinuous pressures. Comput Methods Appl Mech Eng 199:1019–1031. https://doi.org/10.1016/j.cma.2009.11.011

Baumgärtner D, Wolf J, Rossi R, Dadvand P, Wüchner R (2018) A robust algorithm for implicit description of immersed geometries within a background mesh. Adv Model Simul Eng Sci 5(1):21. https://doi.org/10.1186/s40323-018-0113-8

Ben Ahmed S, Dillon-Murphy D, Figueroa C (2016) Computational study of anatomical risk factors in idealized models of type B aortic dissection. Eur J Vasc Endovasc Surg 52(6):736–745

Berguer R, Parodi J, Schlicht M, Khanafer K (2015) Experimental and clinical evidence supporting septectomy in the primary treatment of acute type B thoracic aortic dissection. Ann Vasc Surg 29(2):167–173. https://doi.org/10.1016/j.avsg.2014.10.001

Bhardwaj R, Mittal R (2012) Benchmarking a coupled immersed-boundary-finite-element solver for large-scale flow-induced deformation. AIAA J 50(7):1638–1642. https://doi.org/10.2514/1.J051621

Canchi S, Guo X, Phillips M et al (2018) Role of re-entry tears on the dynamics of type B dissection flap. Ann Biomed Eng 46(1):186–196

Chen H, Peelukhana S, Berwick Z et al (2016) Fluid–structure interaction simulations of aortic dissection with Bench validation. J Vasc Surg 64(6):1892

Codina R, Soto O (2002) A numerical model to track two-fluid interfaces based on a stabilized finite element method and the level set technique. Int J Numer Methods Fluids 40:293–301. https://doi.org/10.1002/fld.277

Dadvand P, Rossi R, Gil M et al (2013) Migration of a generic multi-physics framework to HPC environments. Comput Fluids 80:301–309. https://doi.org/10.1016/j.compfluid.2012.02.004

Dadvand P, Rossi R, Oñate E (2010) An object-oriented environment for developing finite element codes for multi-disciplinary applications. Arch Comput Methods Eng 17(3):253–297. https://doi.org/10.1007/s11831-010-9045-2

Dillon-Murphy D, Noorani A, Nordsletten D, Figueroa CA (2016) Multi-modality image-based computational analysis of haemodynamics in aortic dissection. Biomech Model Mechanobiol 15(4):857–876

Donea J, Huerta A, Ponthot JP, Rodríguez-Ferran A (2004) Arbitrary Lagrangian–Eulerian methods, ch. 14. American Cancer Society, New York

Fattori R, Mineo G, Di Eusanio M (2011) Acute type B aortic dissection: current management strategies. Curr Opin Cardiol 26(6):488–493

Faure E, Canaud L, Cathala P, Serres I, C MA, Alric P (2014) Human ex-vivo model of Stanford type B aortic dissection. J Vasc Surg 60(3):767–775. https://doi.org/10.1016/j.jvs.2013.06.083

François CJ, Markl M, Schiebler ML et al (2013) Four-dimensional, flow-sensitive magnetic resonance imaging of blood flow patterns in thoracic aortic dissections. J Thorac Cardiovasc Surg 145(5):1359–1366

Gravouil A, Moës N, Belytschko T (2002) Non-planar 3D crack growth by the extended finite element and level sets—part II: level set update. Int J Numer Methods Eng 53(11):2569–2586. https://doi.org/10.1002/nme.430

Hartnell G, Gates J (2005) Aortic fenestration: a why, when, and how-to guide. Radiographics 25(1):175–189

Hirt C, Amsden A, Cook J (1974) An arbitrary Lagrangian–Eulerian computing method for all flow speeds. J Comput Phys 14(3):227–253. https://doi.org/10.1016/0021-9991(74)90051-5

Iwai F, Sostman HD, Evans AJ et al (1991) Cine phase-contrast magnetic resonance imaging for analysis of flow phenomena in experimental aortic dissection. Invest Radiol 26(12):1071–1078

Liu D, Fan Z, Li Y et al (2018) Quantitative study of abdominal blood flow patterns in patients with aortic dissection by 4-dimensional flow MRI. Sci Rep 8(1):9111. https://doi.org/10.1038/s41598-018-27249-9

Löhner R, Cebral JR, Camelli FE et al (2008) Adaptive embedded and immersed unstructured grid techniques. Comput Methods Appl Mech Eng 197(25–28):2173–2197

Marconi S, Lanzarone E, De Beaufort H, Conti M, Trimarchi S, Auricchio F (2017) A novel insight into the role of entry tears in type B aortic dissection: pressure measurements in an in vitro model. Int J Artif Organs 40(10):563–574

Nauta FJ, Bogerijen VGH, Conti M et al (2017) Impact of thoracic endovascular repair on pulsatile aortic strain in acute type B aortic dissection. Aorta 5(02):42–52

Nauta FJ, Conti M, Kamman AV et al (2015) Biomechanical changes after thoracic endovascular aortic repair in type B dissection: a systematic review. J Endovasc Ther 22(6):918–933

Osher S, Fedkiw R (2003) Level set methods and dynamic implicit surfaces. Applied mathematical sciences, vol 153, 1st edn. Springer, New York

Peelukhana S, Wang Y, Berwick Z et al (2017) Role of pulse pressure and geometry of primary entry tear in acute type B dissection propagation. Ann Biomed Eng 45(3):592–603. https://doi.org/10.1007/s10439-016-1705-4

Qing KX, Chan YC, Lau SF, Yiu WK, Ting ACW, Cheng SWK (2012) Ex-vivo haemodynamic models for the study of stanford type B aortic dissection in isolated porcine aorta. Eur J Vasc Endovasc Surg 44(4):399–405. https://doi.org/10.1016/j.ejvs.2012.06.004

Rossi R, Larese A, Dadvand P, Oñate E (2013) An efficient edge-based level set finite element method for free surface flow problems. Int J Numer Methods Fluids 71(6):687–716. https://doi.org/10.1002/fld.3680

Rudenick P, Bijnens B, García-Dorado D, Evangelista A (2013) An in vitro phantom study on the influence of tear size and configuration on the hemodynamics of the lumina in chronic type B aortic dissections. J Vasc Surg 57(2):464–474

Rudenick P, Bordone M, Bijnens B et al (2010a) A multi-method approach towards understanding the pathophysiology of aortic dissections—the complementary role of in-silico, in-vitro and in-vivo information. Springer, pp 114–123

Rudenick PA, Bordone M, Bijnens BH, Soudah E, Oñate E, Garcia-Dorado D, Evangelista A (2010b) Influence of tear configuration on false and true lumen haemodynamics in type B aortic dissection. In: 2010 Annual International Conference of the IEEE Engineering in Medicine and Biology, pp 2509–2512. https://doi.org/10.1109/IEMBS.2010.5626689

Ryzhakov P, Soudah E, Dialami N (2019) Computational modeling of the fluid flow and the flexible intimal flap in type B aortic dissection via a monolithic Arbitrary Lagrangian/Eulerian fluid-structure interaction model. Int J Numer Methods Biomed Eng. https://doi.org/10.1002/cnm.3239

Sherrah A, Callaghan F, Puranik R et al (2017) Multi-velocity encoding four-dimensional flow magnetic resonance imaging in the assessment of chronic aortic dissection. AORTA J 5(3):80

Song SW, Yoo KJ, Kim DK, Cho BK, Yi G, Chang BC (2011) Effects of early anticoagulation on the degree of thrombosis after repair of acute DeBakey type I aortic dissection. Ann Thorac Surg 92(4):1367–1375

Soudah E, Rudenick P, Bordone M et al (2015) Validation of numerical flow simulations against in vitro phantom measurements in different type B aortic dissection scenarios. Comput Methods Biomech Biomed Eng 18(8):805–815

Soudah E, Pennecot J, Pérez JS, Bordone M, Oñate E (2011) MedicalGiD: from medical images to simulations, 4D MRI flow analysis. In: Tavares JMRS, Jorge RMN (eds) Computational vision and medical image processing: recent trends. Springer, Dordrecht, pp 145–160. https://doi.org/10.1007/978-94-007-0011-6_8

Sussman M, Smereka P, Osher S (1994) A level set approach for computing solutions to incompressible two-phase flow. J Comput Phys 114(1):146–159. https://doi.org/10.1006/jcph.1994.1155

Tolenaar J, Keulen VJ, Trimarchi S et al (2013) Number of entry tears is associated with aortic growth in type B dissections. Ann Thorac Surg 96(1):39–42. https://doi.org/10.1016/j.athoracsur.2013.03.087

Tsai TT, Evangelista A, Nienaber CA et al (2007) Partial thrombosis of the false lumen in patients with acute type B aortic dissection. N Engl J Med 357(4):349–359

Tsai T, Schlicht M, Khanafer K et al (2008) Tear size and location impacts false lumen pressure in an ex vivo model of chronic type B aortic dissection. J Vasc Surg 47(4):844–851. https://doi.org/10.1016/j.jvs.2007.11.059

Tse KM, Chiu P, Lee HP, Ho P (2011) Investigation of hemodynamics in the development of dissecting aneurysm within patient-specific dissecting aneurismal aortas using computational fluid dynamics (CFD) simulations. J Biomech 44(5):827–836

Wan AB Naim W, Ganesan P, Sun Z, Osman K, Lim E (2014) The impact of the number of tears in patient-specific Stanford type B aortic dissecting aneurysm: CFD simulation. J Mech Med Biol 14(02):1450017

Winter M, Schott B, Massing A, Wall W (2018) A Nitsche cut finite element method for the Oseen problem with general Navier boundary conditions. Comput Methods Appl Mech Eng 330:220–252. https://doi.org/10.1016/j.cma.2017.10.023

Yazdani A, Li H, Bersi MR et al (2018) Data-driven modeling of hemodynamics and its role on thrombus size and shape in aortic dissections. Sci Rep 8(1):2515

Zorrilla R, Larese A, Rossi R (2019) A modified finite element formulation for the imposition of the slip boundary condition over embedded volumeless geometries. Comput Methods Appl Mech Eng 353:123–157. https://doi.org/10.1016/j.cma.2019.05.007